

# A Geometric Model for 3-D Confocal Image Analysis

Alessandro Sarti, Carlos Ortiz de Solórzano, *Member, IEEE*, Stephen Lockett, and Ravikanth Malladi\*

**Abstract**—In this paper, we use partial-differential-equation-based filtering as a preprocessing and post processing strategy for computer-aided cytology. We wish to accurately extract and classify the shapes of nuclei from confocal microscopy images, which is a prerequisite to an accurate quantitative intranuclear (genotypic and phenotypic) and internuclear (tissue structure) analysis of tissue and cultured specimens. First, we study the use of a geometry-driven edge-preserving image smoothing mechanism before nuclear segmentation. We show how this filter outperforms other widely-used filters in that it provides higher edge fidelity. Then we apply the same filter, with a different initial condition, to smooth nuclear surfaces and obtain sub-pixel accuracy. Finally we use another instance of the geometrical filter to correct for misinterpretations of the nuclear surface by the segmentation algorithm. Our prefiltering and post filtering nicely complements our initial segmentation strategy, in that it provides substantial and measurable improvement in the definition of the nuclear surfaces.

**Index Terms**—Cytology, differential geometry, dynamic surfaces, image processing, level sets, Riemannian geometry, segmentation, surface evolution.

## I. INTRODUCTION

CYTOLOGY shows that the cells in a tissue become increasingly heterogeneous in their structural properties during carcinogenesis, while histology shows increasing disorganization of the cells. Furthermore, whether a precancerous or cancerous lesion progresses, is stable or enters remission is likely to depend on the chemical and physical environment of the cell in the lesion [9], [12], [20] in addition to the internal properties of the cells. In order to understand these structural alterations, together with the molecular mechanisms underlying them, it is necessary to analyze the cells individually and within their natural tissue context. Since many of the structural and molecular changes occur within the cell's nucleus, the ability to segment the individual nuclei in intact tissue is therefore an important and basic technical capability.

Manuscript received March 24, 1999; revised July 19, 2000. This work was supported by the U.S. Department of Energy's Office of Energy Research, Office of Computational and Technology Research, Mathematical, Information, and Computational Sciences Division, Applied Mathematical Sciences Subprogram; Director, Office of Energy Research, Office of Health and Environmental Research under Contract DE-AC03-76SF00098; by the Office of Naval Research (ONR) under Grant N00014-96-1-0381; and by LBNL Directed Research and Development Program. This work was also supported by the U.S. National Institutes of Health (NIH) under Grant CA-67412, a contract with Zeiss Inc., and by the Training program in Genome Research of the UC Systemwide Biotechnology Research and Education Program. Asterisk indicates corresponding author.

A. Sarti, C. Ortiz de Solórzano, and S. Lockett are with Lawrence Berkeley National Laboratory, University of California, Berkeley, CA 94720 USA (e-mail: {asarti; malladi}@math.lbl.gov; {carlos; lockett}@black.lbl.gov).

\*R. Malladi is with Lawrence Berkeley National Laboratory, University of California, MS 50A-1148, 1 Cyclotron Road, Berkeley, CA 94720 USA (e-mail: malladi@math.lbl.gov).

Publisher Item Identifier S 0018-9294(00)10194-6.

To obtain quantitatively accurate measurements at the individual nucleus level, it is necessary to analyze intact nuclei. Therefore, thick ( $>20\ \mu\text{m}$ ) sections must be employed, which requires three-dimensional (3-D) (confocal) microscopic image acquisition [34] followed by 3-D image analysis. In order to facilitate the segmentation of nuclei from images, it is usual to label the specimen with a fluorescent DNA counterstain, because it produces very high contrast images containing high intensity nuclear regions versus low intensity nonnuclear (background) regions. Actual segmentation of nuclei can be obtained by either interactive or automatic algorithms. Interactive methods, based on drawing around nuclei in sequence [6], [25] or orthogonal [13] 2-D slices are superior in performance (defined as the fraction of nuclei correctly segmented) based on visual judgment of the results compared to automatic algorithms. However, they are slow, tedious, and require intense human effort, typically taking many minutes per nucleus and are thus limited in their practical application to situations where only few nuclei require analysis.

Automatic algorithms [3], [10], [23], on the other hand are much faster, enabling the analysis of hundreds of nuclei per study: The performance of the automatic methods is only high ( $>90\%$ ) for specimens containing isolated nuclei. Moreover, performance significantly deteriorates for many cancer specimens, because the cells are structurally dominated by their nuclei leaving little separating cytoplasm and thus the images show clustered nuclei.

This is the kind of biological specimen we are interested to study and therefore the accuracy of the segmentation method calls for improvement. To this end, the 3-D segmentation approach in [23] combines the speed of automatic image analysis algorithms with the performance of interactive algorithms by including visual inspection stages in the method. This enables the correct segmentation of a high proportion of individual nuclei in intact tissue, while greatly reducing user effort and providing comparable accuracy to that of manual methods for segmenting cell nuclei. However, the method still needs improvements by way of better edge fidelity especially for clusters of highly irregular nuclei and for nuclei with highly uneven DNA staining.

Encouraged by the recent advances [15]–[18], [33], [2], [26], [29], [19] in partial-differential-equation-based image analysis tools, in this paper, we extend and apply some of those methods to confocal microscope image analysis. Specifically, we are interested in first preprocessing a given 3-D image to reduce noise by paying close attention to the edge geometry, and then expressing the nuclear segmentation as the solution of an initial valued partial differential equation. We show the benefit of using the geometric method via a detailed comparison to other methods and tabulating the measurements under a variety of noise conditions on both synthetic and real confocal images.

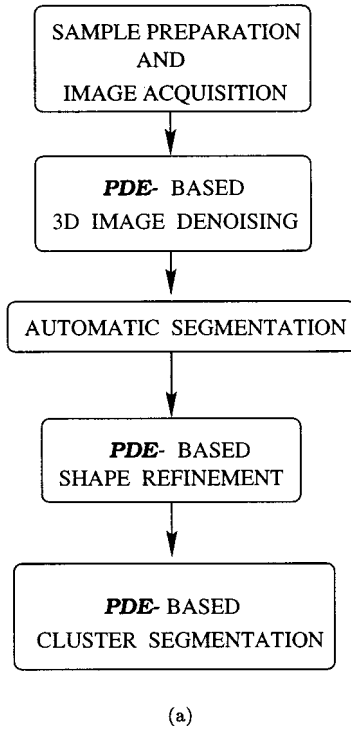


Fig. 1. Flowchart depicting the sequence of steps we undertake.

The theme of this paper is to start with a governing equation that is expressed via an Euler–Lagrange of a functional and to exploit some of its many interpretations to perform edge-preserving image denoising and shape extraction in three dimensions. Other tasks to complete the chain include curvature-based min-flow to rid a given shape of its holes, and to split nuclear clusters in order to re-classify them [30]. Various forms of our equation are then implemented using the level set [24] methods and the efficient narrow-band versions [1], [15] of it. The flowchart in Fig. 1 shows the exact sequence of steps we undertake in order to analyze a 3-D confocal microscope image. In the present context, we address the first four steps of this flow chart.

The rest of the paper is organized as follows: in Section II we review some previous work on our automatic segmentation method. This sets the stage for the work to follow on partial-differential-equation-based methods. In Section III, we introduce the main equation and we outline its relevant features. In Section IV, we interpret the main equation as an image processing algorithm and show its application to confocal microscope image denoising. In this section, we also quantify the benefit of employing the geometric filter for image processing by comparing its performance with that of median and morphological filters. In Section V, we examine the geometric interpretation of our main model and show that it can be used for shape refinement and correction.

## II. PREVIOUS WORK

A typical image contains a large number of nuclei (upto 1500–2500 separate nuclei). Therefore, any segmentation approach has to be automatic requiring minimal user intervention. But, as we pointed out in the introduction, automatic methods

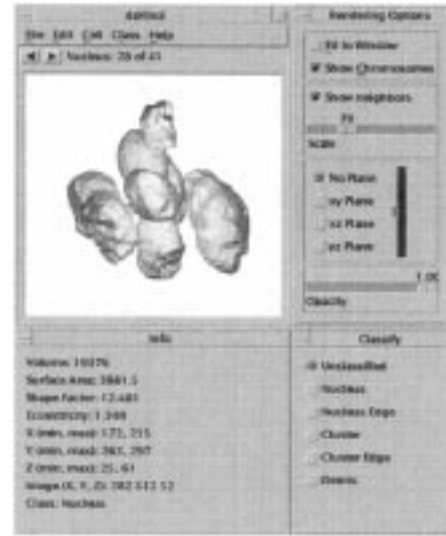


Fig. 2. DaVinci User Interface. (1) Top Left Panel: 3-D graphics window showing some nuclei; (2) Top Right: Surface rendering options (3) Bottom Left: Quantitative Object Information; (4) Bottom Right: Object Classification Panel.

also suffer from lack of accuracy. Therefore, we propose a hybrid approach that starts with an automatic segmentation method and improves the result by doing PDE-based post processing.

In order to make the scheme clear, we follow some of the work in [23] and briefly summarize the automatic segmentation method to get a rough estimate of nuclear shapes and the subsequent steps of cluster division and object classification. The algorithm works as follows: First, an adaptative, gradient weighted averaged thresholding is used to extract nuclear stained DNA volumes from the unstained background. The call for using an adaptative versus fixed threshold is justified by the variation in image intensity in the focus ( $Z$ ) axis typical of confocal imaging of thick sections. This heterogeneity is due to increasing scattered light, photobleaching and loss of refractive index coupling between the medium and the rest of the optical path as we image deeper tissue sections. After thresholding, the user visualizes and classifies each segmented volume as being a nucleus, cluster of nuclei or debris, using a 3-D visualization program: Data Visualization ANd Computer Interaction (DaVinci) developed in house. DaVinci (Fig. 2) provides quantitative information about the rendered object and a variety of interaction tools (zooming, intersection of the rendered surface with 2-D slices from the original 3-D image, rotation, surface opacity control, etc.) to help the user to classify the object.

Objects classified as clusters are divided into sub-components using a series of automatic algorithms: First, the vector distance transform (VDT) of the cluster's binary mask is calculated and the peaks of this transform are used as internal markers for individual nuclei inside the cluster. Next, the inverse of either the VDT (option 1) or the original grayscale image (option 2) is used for the flooding process of a watershed algorithm to find surfaces between nuclei in the cluster. The sub-components resulting from the cluster segmentation are reclassified by the user. Incorrectly divided individual nuclei can then be rejoined.

The algorithm was tested on 2500 nuclei from five different types of samples that covered a range of segmentation difficulty levels. Specimens of nondensely clustered and approximately spherical nuclei could be easily segmented (99% of nuclei were correctly segmented based on visual verification). For specimens where nuclei were more clustered and variable in shape, performance deteriorated. For normal appearing human breast tissue it was 90%, but it was lower for cancerous tissue. However, the point to emphasize about the performance is that while not all nuclei in a specimen were segmented, the inclusion of the visual classification step meant that it was known which nuclei were correctly segmented and which were not.

#### A. Limitations of the Previous Method

We have identified two main sources of error in our current segmentation method: 1) In the initial automatic thresholding, inaccurate surface definition is caused by a low Signal to Noise Ratio of the acquired image, 2) In the watershed-based cluster segmentation algorithm, erroneous surface delineation occurs when there is not enough morphological (option 1) or gradient (option 2) information in the image to correctly lead the segmentation procedure. In the following sections, we present a unified geometric image denoising/enhancing/optimization scheme that addresses both problems.

### III. GEOMETRIC MODEL FOR IMAGE ANALYSIS

In this section, we introduce a geometric model; various forms of this equation are used in this paper in order to implement our image analysis procedures. The method relies on estimating the motion of curves and surfaces that move in the normal direction with a given speed. Given a hypersurface  $\gamma(\mathbf{x})$  that is moving under speed  $F(\mathbf{x})$ , we adopt the level set equation to represent its motion [24], [31], [32]. In other words, we embed the hypersurface as the zero level set of a higher dimensional function  $\psi(\mathbf{x})$ , and write the following equation of motion by following the chain rule:

$$\psi_t + F|\nabla\psi| = 0 \quad (1)$$

with a given initial condition  $\psi(\mathbf{x}, t = 0) = \psi_0$ . This approach is an alternative to writing the equations of motion for the parameterized representation of the curve or the surface [11]. As pointed out in [24], the level set approach offers several advantages. First, although the higher dimensional function remains a function, its zero level set can change topology, and form sharp corners. Second, a discrete grid can be used together with finite differences to devise a numerical scheme to

approximate the solution. Third, intrinsic geometric quantities like normal and curvature of the curve can be easily extracted from the higher dimensional function. Finally, everything extends directly to moving surfaces in three dimensions.

This model of curve and surface motion has been applied to the problem of shape modeling in [14], [4], [15], [17]. Imagine that one is given an image and the problem is to extract boundary descriptions of all the shapes implicitly present in it. The approach in [15] is one of using a trial shape that propagates in the image domain and molds itself into the desired boundary. The speed function used to control this shape recovery process is a combination of constant inflationary speed, a geometry dependent speed that regularizes the final result, and an image-dependent speed. Specifically, the equation of motion is given by

$$\psi_t + g(1 - \epsilon H)|\nabla\psi| = 0 \quad (2)$$

where  $g$  is a decreasing function of the image gradient and  $H$  is the mean curvature. For example, the function  $g(\mathbf{x}) = e^{-\alpha|\nabla G_\sigma * I(\mathbf{x})|}$ ,  $\alpha > 0$  was used in [15]. In other words, the function  $g$  is designed so that its values are closer to zero at high image gradients, i.e., likely edges. An additional forcing term can be added to this equation to improve the accuracy in the presence of large variations in image gradient. This is often realized by advecting the surface along an image dependent vector field [5], [17]; the force field is synthesized in such a way that it always points in the edge direction. With this change, our equation becomes

$$\psi_t + g(1 - \epsilon H)|\nabla\psi| - \beta \nabla g \cdot \nabla\psi = 0. \quad (3)$$

In [5], the shape computation has been posed as a weighted area minimization problem and (3) as a necessary condition to obtain minimum of the energy  $A = \iint g(I(\mathbf{x})) da$ , where  $da$  is the area element. This equation is then solved with the initial condition  $\psi(\mathbf{x}, t = 0) = \pm d(\mathbf{x})$ , where  $d$  is the distance function computed in the domain off the user-defined initial hypersurface  $\gamma$ . The equation is approximated with finite differences and solved using the following iterative scheme; see [24], [32] for details. In two-dimensions, consider a uniform grid and let  $\psi_{ij}^n$  be the value of the function  $\psi$  at time  $n\Delta t$  and at the point  $(i\Delta x, j\Delta y)$ . With this notation, the update equation is shown in (4) at the bottom of the page, where  $D$  is a finite difference operator on  $\psi$ , the superscripts  $\{-, 0, +\}$  indicate backward, central and forward differences respectively, and the superscripts  $\{x, y\}$  denote the direction of differentiation. Again, the key advantages of our geometric model over other shape recovery scheme are its topo-

$$\psi_{ij}^{n+1} = \psi_{ij}^n + \Delta t \left[ \begin{aligned} & \left[ g_{ij} H_{ij}^n \left( D_{ij}^{0x^2} + D_{ij}^{0y^2} \right)^{1/2} \right] \\ & - g_{ij} \left\{ \max(D_{ij}^{-x}, 0)^2 + \min(D_{ij}^{+x}, 0)^2 + \max(D_{ij}^{-y}, 0)^2 + \min(D_{ij}^{+y}, 0)^2 \right\}^{1/2} \\ & + \beta \left\{ \begin{aligned} & [\max(g_{ij}^{0x}, 0) D_{ij}^{-x} + \min(g_{ij}^{0x}, 0) D_{ij}^{+x}] \\ & + \max(g_{ij}^{0y}, 0) D_{ij}^{-y} + \min(g_{ij}^{0y}, 0) D_{ij}^{+y} \end{aligned} \right\} \end{aligned} \right]. \quad (4)$$

logical adaptability, robust numerics, and fast real-time implementations [18] on dense multidimensional data.

#### IV. IMAGE DENOISING

In this section, we are interested in denoising or improving the signal-to-noise ratio (SNR) of a given image. This is an essential step in image analysis specially in high noise situations that can disrupt the shape information. Image denoising has two principal requirements. One is to smooth all the homogeneous regions that contain noise and the other is to retain in an accurate way the location of the boundaries that define the shape of the represented structures. The application of traditional pre-processing algorithms (moving average, median and Gaussian filtering) do reduce the noise superimposed on the image but do not maintain a good definition of the edges or image features. Furthermore, in biomedical imaging, noise is due to different causes, and is difficult to model. In particular, the concentration variation of the fluorescence labeled molecules (in this case DNA) superimposes a de facto noise level that is difficult to model.

We now show how we can use (3) to denoise images. The basic idea is to delete the constant speed term and solve the equation with the noisy image as the initial condition, namely

$$\psi_t = gH|\nabla\psi| + \beta\nabla g \cdot \nabla\psi \quad (5)$$

with  $\psi(\mathbf{x}, t = 0) = I_0(\mathbf{x})$ . So, we are moving the level curves or the iso-intensity contours/surfaces of a given image in the normal direction with curvature-dependent speed and attracting them toward local edges as specified by the edge indicator function  $g$ . The first term on the right in the above equation is a parabolic smoothing term and the second is a hyperbolic term. The proposed model is a selective smoothing of the 3-D image, where the edges are preserved as much as possible. The indicator function  $g$  allows us to decide whether a detail is strong enough to be retained. In our model,  $g$  is a smooth nonincreasing function of the initial image  $I_0(\mathbf{x})$ , namely

$$g = g(|\nabla(G \star I_0(\mathbf{x}))|) \quad (6)$$

where  $G(\mathbf{x})$  is a Gauss kernel and the symbol  $\star$  denotes convolution.

In particular,  $g(0) = 1$ ,  $g(|\nabla(G \star I_0(\mathbf{x}))|) \geq 0$ , and  $\lim_{|\nabla(G \star I_0(\mathbf{x}))| \rightarrow \infty} g(|\nabla(G \star I_0(\mathbf{x}))|) = 0$ . Typical forms of  $g(|\nabla(G \star I_0(\mathbf{x}))|)$  are

$$g(|\nabla(G \star I_0(\mathbf{x}))|) = e^{-(|\nabla(G \star I_0(\mathbf{x}))|/\gamma)} \quad (7)$$

or

$$g(|\nabla(G \star I_0(\mathbf{x}))|) = \frac{1}{1 + \frac{|\nabla(G \star I_0(\mathbf{x}))|}{\gamma}}. \quad (8)$$

The smoothing works as follows: if  $|\nabla(G \star I_0(\mathbf{x}))|$  is large, the flow is slow and the exact location of the edges will be retained. If  $|\nabla(G \star I_0(\mathbf{x}))|$  is small then the flow tends to be fast thereby increasing the smoothing process. Notice that the filtering model reduces to mean curvature flow when  $g(s) = 1$ . It is important to note here that the  $g$  function depends on the initial image  $I_0$  and serves as an edge indicator. The reason the

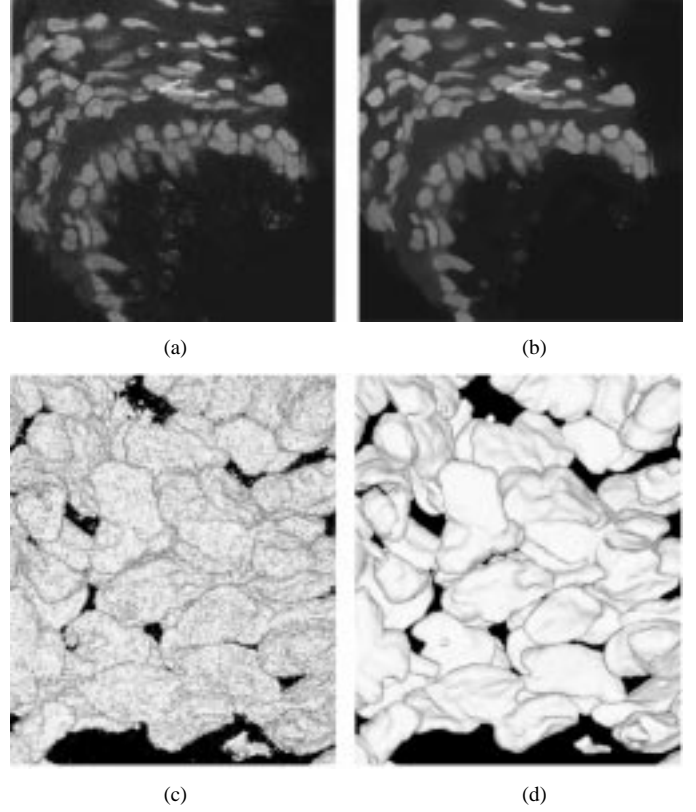


Fig. 3. Two-dimensional and 3-D edge-preserving smoothing and edge sharpening results; (a) 2-D slice of the unfiltered image, and (b) Geometric image processing with  $\beta = 1$  and  $\sigma = 1$ . (c) Surface rendering representation of the unfiltered volume, and (d) Geometric image processing with  $\beta = 1$  and  $\sigma = 1$ .

initial image  $I_0$  is convolved with a Gaussian low pass filter is to eliminate the influence of spurious noise related edges in  $g$ . But a robust edge definition is what we are attempting to compute by solving (5). So, the way out of this cyclical dependence is to make  $g$  a function of time  $t$  and to recompute it at every time step of our iterative solution scheme. Therefore,  $g$  is a function of  $|\nabla I(\mathbf{x}, t)|$ . We start with a crude approximation of the edge indicator function in (5) and progressively improve it while solving the equation. As time progresses, the image becomes smoother and smoother, and the edge indicator function  $g$  depends less and less on spurious noise.

On the other hand, if we can fix the size of the minimal image detail, a static  $g$  function can be synthesized by simply smoothing the initial image with a Gaussian smoothing kernel. We note here that the minimal size of the detail is related to the size of the Gauss kernel, which acts like a scale parameter. In fact, the variance of  $G_\sigma(\mathbf{x}) = (1/C_\sigma)e^{-(|\mathbf{x}|^2/4\sigma)}$  corresponds to the dimension of the smallest structures that have to be preserved. The second (hyperbolic) term in (5) sharpens the edge information in the image; note that a similar observation was made in [27].

Now we present some results. Fig. 3(a) is a benign region of a breast cancer specimen, labeled with a fluorescent stain (propidium iodide) for identification of the cell nuclei. The lower bilayer of nuclei are in epithelial cells and are surrounding a duct. Fig. 3(b) shows the result of solving (5) with the image itself as an initial condition; Fig. 3(c)–(d) shows the result of 3-D

TABLE I  
COMPARISON BETWEEN MORPHOLOGICAL, MEDIAN AND THE GEOMETRIC FILTER

	Numerical Objects			Cell Shapes			Fluorescent Beads		
Noise Level	Morphological	Median	Geometric	Morphological	Median	Geometric	Morphological	Median	Geometric
N0	0	0	0	0.06	0.04	0	0.16	0.17	0.11
N1	0.01	0.02	0	0.06	0.04	0	0.24	0.20	0.26
N2	0.01	0.04	0	0.06	0.04	0.02	0.34	0.44	0.15
N3	0.02	0.46	0	0.06	0.04	0.02	0.48	0.68	0.30
N4	0.05	0.80	0.02	0.07	0.04	0.03	0.60	0.83	0.31
N5	0.07	1.03	0.08	0.09	0.15	0.04	0.91	0.99	0.24
N6	0.09	1.22	0.05	0.13	0.19	0.06	1.09	1.19	0.32
N7	0.11	1.39	0.11	1.16	0.22	0.08	1.16	1.33	0.36
N8	0.51	1.45	0.20	4.49	0.25	0.12	1.22	1.51	0.30
N9	1.91	1.47	0.33	5.87	0.29	0.16	1.32	1.70	0.40
N10	3.77	1.47	0.50	6.34	0.36	0.19	1.40	1.84	0.44

edge-preserving smoothing on a portion of the confocal microscope image volume.

#### A. Noise Reduction: Validation Study

We observe from visual inspection of the results in Fig. 3 that the noise is significantly reduced while the nuclear boundaries or the edge information is kept sharp and intact. Since visual inspection is not known to be reliable, in this section, we go a step further and attempt to quantify the performance of our geometric filter. We compare the improvement achieved by the geometric flow filter with that provided by a median filter. The comparison is done in the following way: we first segment a noise-free image and treat that segmentation as our reference. Every instance of a noise-added image is then denoised using three filters, morphological (opening and closing operations with a kernel size  $3 \times 3$ ), median and our geometric filter. The shapes are then segmented from these images and compared to the reference shape. This is done by identifying every voxel on the surface of the reference object and calculating its distance in voxels to the closest voxel on the surface of the object segmented from noise-added image. The average of this set of closest distance is calculated to produce numbers that are comparable across different noise levels. Several levels of noise has been added to the test images to show the robustness of the filter. The noise that is added to every image point is uniformly distributed; for the noise level  $N_i$ , the maximum value of additive noise is set to  $i\%$  of the maximum image intensity level. Finally, the figures are tabulated in Table I for all noise levels and all the test images.

In our experiment, we have used three image types.

- 1) Synthetic objects (Fig. 4): We first work on an image populated with computer-generated objects. The shapes are generated using the superquadric equation. The equation  $S(x, y, z) = (x/a)^{2/\epsilon_1} + (y/b)^{2/\epsilon_2} + (z/c)^2 - 1$  implicitly defines a superquadric, which represents a family of shapes that is much more diverse compared to an ellipsoid due to the addition of “squareness” parameters.
- 2) Cell-shaped object (Fig. 5): A better understanding of the effect of the filter can be obtained from objects resembling the shape of real cell nuclei. Since it is impossible to obtain a measurement of the cell surfaces in real images (prior to segmentation), we created models of real images from the object that is a result of segmenting an image containing DNA counterstained nuclei. The binary

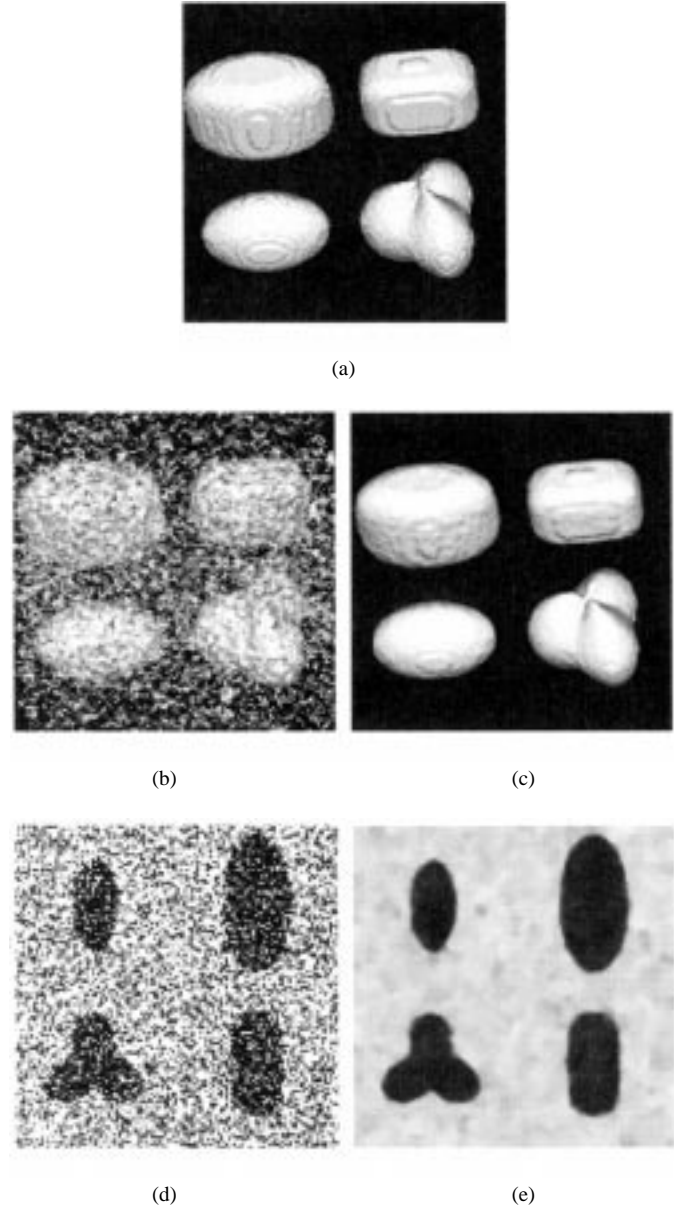


Fig. 4. Three-dimensional numerical phantoms: (a)–(c) Numerical phantoms with uniform noise distribution (50% of the peak) and the result of the geometric filtering; (d)–(e) Noisy (100% uniform distributed) and filtered orthogonal slice from the 3-D phantom. (a) Original, (b) 50% noise added, (c) restored, (d) 100% noise added, and (e) restored.

segmented image was multiplied by 200 and noise was added as we did before.

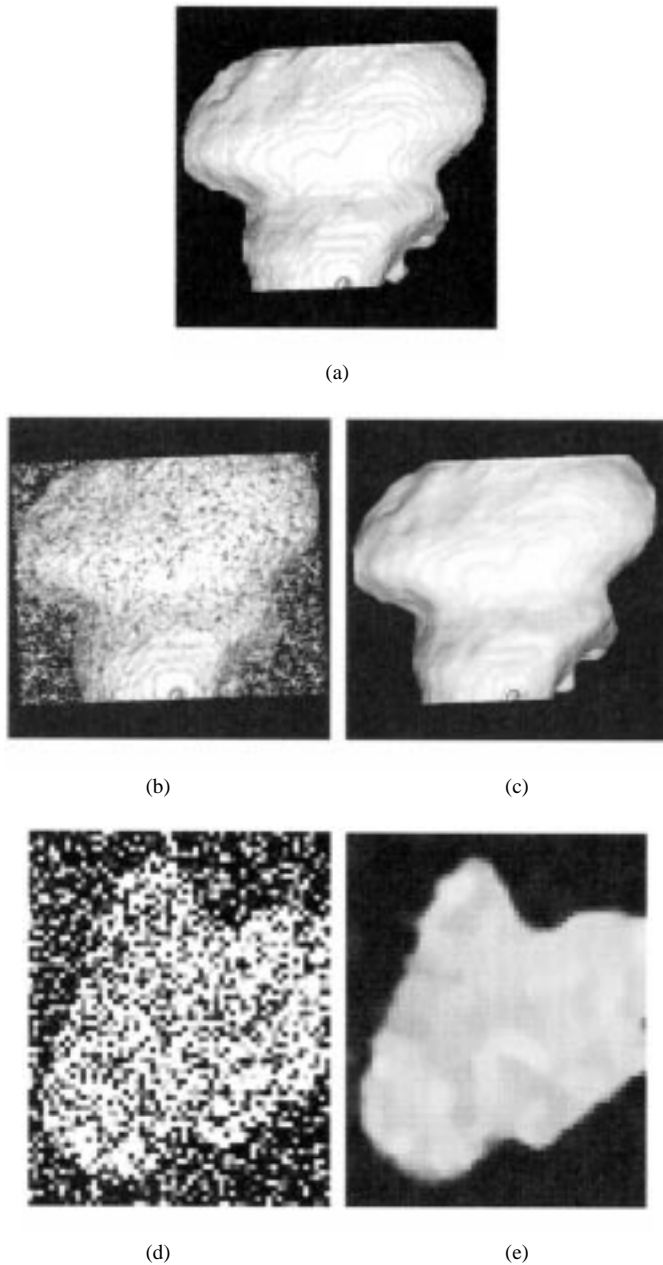


Fig. 5. Cell shaped object: (a)–(c), Noise corrupted (50% uniform distribution) and filtered cell shaped objects; (d)–(e), Noisy (100% uniform distribution) and filtered orthogonal slice from the 3-D volume of cell shaped object. (a) Original, (b) 50% noise added, (c) restored, (d) 100% noise added, and (e) restored.

- 3) Confocal images of fluorescent beads (Fig. 6). To introduce the effect of the Optical response of the microscope in our comparison, we used real confocal images of fluorescent microspheres. The images were acquired using a Zeiss LSM/410 confocal microscope and stored in the ICS file format before analysis.

The error in the segmentation from a noisy image is calculated as follows: first we estimate the surface of the object from noise-free image as the intersection between the original binary image and a 3-D morphological erosion of them, using a  $3 \times 3$  kernel. Then the VDT [21] (Vector Distance Transform) of the noise-free objects is computed; this assigns to all the voxels in the image a value that is the shortest distance to the surface of

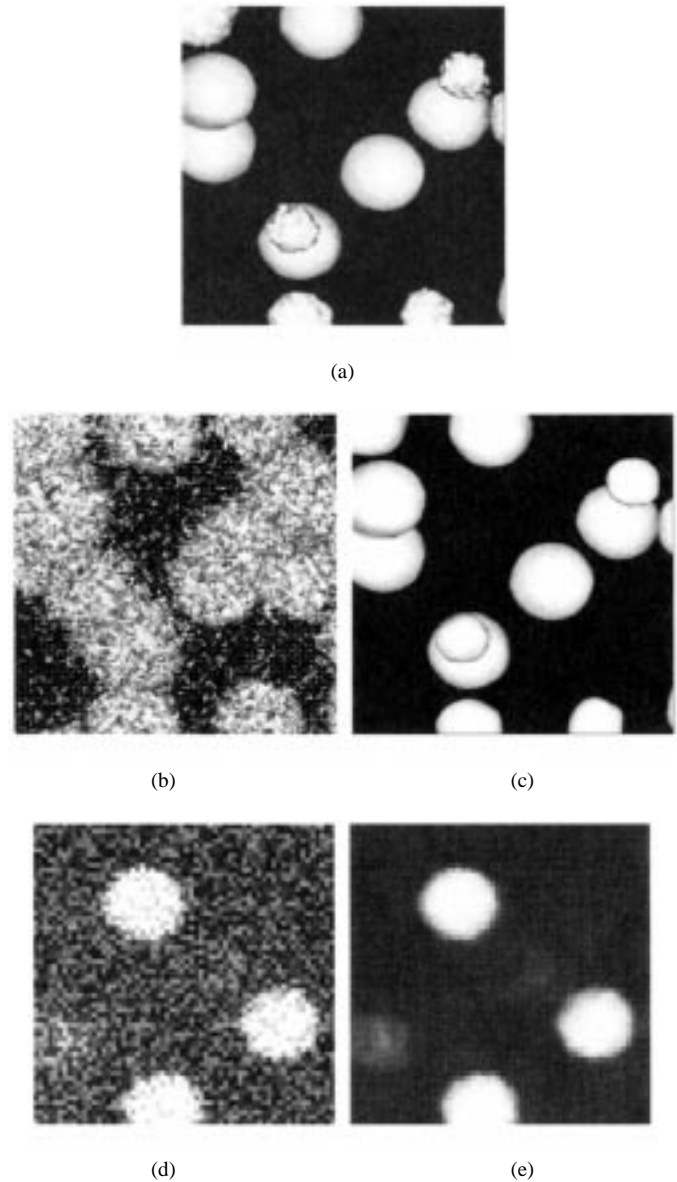


Fig. 6. Fluorescent beads: (a)–(c), Fluorescent beads with 50% of uniform noise distribution and the result of the geometric filtering; (d)–(e), Noisy (50% uniform distribution) and filtered orthogonal slice from the 3-D volume of fluorescent beads. (a) Original, (b) 50% noise added, (c) restored, (d) 100% noise added, and (e) restored.

the objects. Finally, the product of the VDT with the surface segmented from the noise-added image gives us a new image where each nonzero voxel value contains the distance from the noisy surface to the noise-free objects. Fig. 7 provides a graphical explanation of the error computation; the solid line represents (in two dimensions) the surface of our noise-free segmentation and the dotted line represents the surface of the test candidate with a given amount of noise. The numbers on the test surface as one traverses it are the shortest distance to the noise-free segmentation. The average distance is then calculated by adding all the distance values and dividing the sum by the surface area of the reference objects. As depicted in Table I, the error corresponding to our geometric filter are significantly lower compared to those that result from applying a morphological or a median filter. In Fig. 8, we plot the error from the Fluorescent

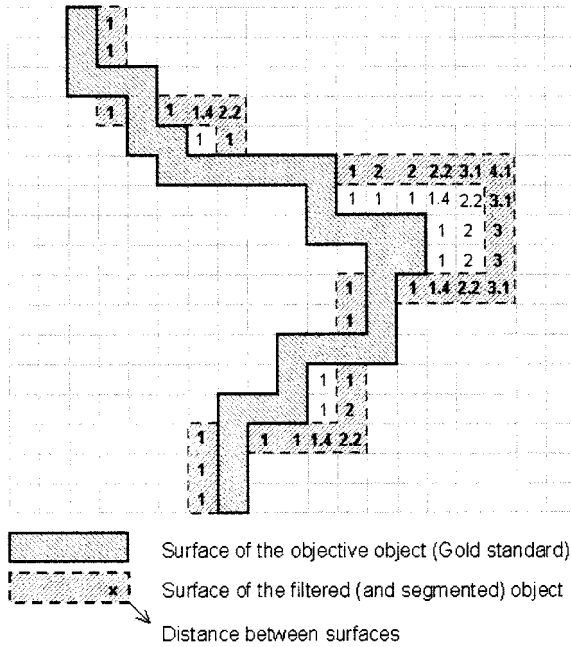


Fig. 7. A graphical explanation of the error computation.

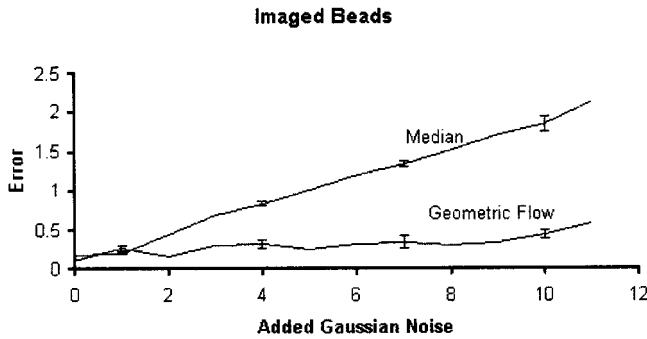


Fig. 8. Error comparison on the Fluorescent beads image.

bead image. Note that the geometric filter error is  $\leq 0.5$ , implying that the residual error is dominated by “voxelization” of the image and not noise; we address this issue in Section VI.

Next, we do another experiment with sections of real confocal microscope images; no artificial noise was added to these image samples. Three different images were used, obtained from specimens consisted on tissue biopsies taken from human or mouse tissue repositories, namely:

- 1) Human skin specimens ( $S$ ) [Fig. 9(a)] were obtained from the archives of the Dermatopathology Sections of the Departments of Pathology and Dermatology, University of California, San Francisco. The specimens were fixed in 10 paraffin-embedded before receipt. The tissue blocks were cut into 20- $\mu\text{m}$  sections stained with PI at 0.1 mg/mL, and mounted in glycerol.
- 2) Human breast specimens containing invasive carcinoma *in situ* parts ( $I$ ) [Fig. 9(b)] were obtained from the Department of Pathology, California Pacific Medical Center (CPMC), San Francisco. They were fixed, embedded and sectioned as described for the skin specimens.

- 3) Formalin-fixed, paraffin embedded MCF7 cells (a human breast cancer cell line) that had been grown in nude mice as a xenograft ( $X$ ) [Fig. 9(c)] were provided by Dr. G. Colbern (Geraldine Brush Cancer Research Institute, CPMC). The xenografts were cut to 30- $\mu\text{m}$  thickness, stained using YO-PRO-1 (Molecular Probes, Eugene, OR), and mounted on glycerol.

Specimens  $S$  were imaged using an MRC-1000 confocal imaging system (Bio-Rad Microscience Ltd. Hemel Hempstead, U.K.) equipped with a Diaphot 200 microscope (Nikon Inc., Instrument Group, Garden City, NY) a 60 $\times$ , 1.4 Plan Apo objective lens (Nikon) and an Argon/Krypton (Ar/Kr) laser. Specimens  $I$  &  $X$  were imaged using a laser scanning confocal microscope 410 (Carl Zeiss Inc., Thornwood, NY) equipped with an Axiovert 100 microscope (Zeiss), a  $\times 63$ , 1.4 NA plan-Achromat objective lens (Zeiss) and an Ar/Kr laser.

The PI in specimens  $S$  &  $I$  was imaged using the 568 nm laser line and collecting emissions longer than 590 nm. The YO-PRO-1 in  $X$  was excited using the 488 nm laser and emissions were detected using a band-pass filter in the range of 515–565 nm. The distance between adjacent 2-D slices was 0.3  $\mu\text{m}$  for  $X$  and 0.5  $\mu\text{m}$  for  $S$  &  $I$ . Voxel size was 0.18  $\mu\text{m}$  in the lateral direction for  $S$  and 0.2  $\mu\text{m}$  for  $I$  and  $X$ . Three images were acquired, one of each type, with sizes 128  $\times$  128  $\times$  40( $S$ ), 128  $\times$  128  $\times$  40( $I$ ) and 512  $\times$  512  $\times$  40( $X$ ), and stored in ICS image format [7] and transferred to a UNIX workstation for archiving and analysis.

The images are first enhanced by solving (5) with  $\beta = 0.1$  and  $\sigma = 1.0$ , and then we compute the SNR. We used the following formula to compute the SNR:  $\text{SNR} = (|m_o - m_b| / \sqrt{\sigma_o^2 + \sigma_b^2})$ , where  $m_o$  and  $m_b$  are the mean signal, and  $\sigma_o$  and  $\sigma_b$  are the standard deviations of the object and the background respectively. The SNR has been computed in three different regions for every specimen and therefore the mean SNR has also been evaluated. The result of this comparison has been tabulated in Table II. The last column contains the gain in SNR due to the geometric filtering, computed as the ratio  $\text{SNR}_{\text{filtered}} / \text{SNR}_{\text{original}}$ . The mean gain for the three specimen is 2.01, so the filtering doubles the SNR.

## V. SEGMENTATION AND SHAPE REFINEMENT

As shown in Fig. 10(a), the resulting surfaces from our automatic segmentation algorithm can be quite coarse with a lot of “voxelization.” This is due to the fact that a thresholding-based segmentation is a binary representation of a surface that either includes or excludes a given point as being in or out of the surface. This process produces an erroneous representation as the shape boundaries shown may be a little away from the true edges. We wish to correct this by refining the shapes using the geometrical flow introduced in previous sections. As we will show, the flow-based equation also makes it possible to represent the final surface with a sub-grid accuracy that is not possible with a threshold-based segmentation. To this end, let us revisit (3), from the geometrical point of view of achieving boundary detection.

Let  $S$  be a surface and assume that it is a particular level set of a function  $\psi : [0, a] \times [0, b] \times [0, c] \rightarrow R$ . In other words,  $S$  is a

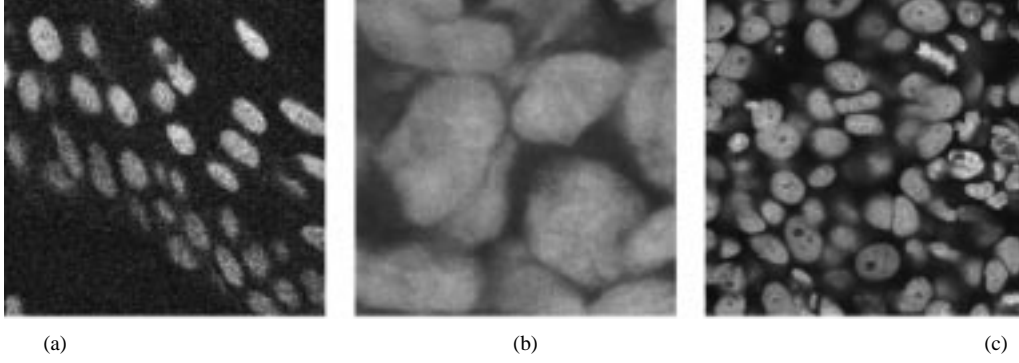


Fig. 9. A 2-D slice of each one of three real confocal microscope images that we used in our study; (a) Human skin specimens ( $S$ ), (b) Human breast specimens ( $I$ ), and (c) Formalin-fixed, paraffin embedded MCF7 cells ( $X$ ).

TABLE II  
COMPARISON BETWEEN SNR BEFORE AND AFTER FILTERING OF 3 SPECIMEN OF THREE DIMENSIONS CONFOCAL IMAGES

Object	Region 1		Region 2		Region 3		Mean		Gain
	Original	Filtered	Original	Filtered	Original	Filtered	Original	Filtered	
Skin Sample ( $S$ )	4.90	18.34	2.67	5.16	3.27	5.38	3.60	9.62	2.67
Mice Sample ( $X$ )	3.89	4.69	8.17	16.54	5.17	8.27	5.75	9.83	1.70
Breast Sample ( $I$ )	4.08	6.60	3.68	6.04	-	-	3.8	6.32	1.66

set of points at which the function  $\psi$  is equal to a given constant. The embedding function  $\psi$  can therefore be considered as an implicit representation of the surface  $\mathcal{S}$ . It is easy to prove that if a surface  $\mathcal{S}$  evolves according to

$$\mathcal{S}_t = F\vec{\mathcal{N}} \quad (9)$$

where  $\vec{\mathcal{N}}$  is the unit inward normal and  $F$  is a real function, then the level set function  $\psi$  obeys the following evolution rule:

$$\psi_t = F|\nabla\psi| \quad (10)$$

see [24] and [31] for details.

Our first objective is to produce a smoother representation of the surface using the above equation. In order to smooth a surface, we can let the speed  $F$  be equal to its mean curvature  $H$ . The flow decreases the total curvature and has the property of “smoothing out” all the high curvature regions on the surface, i.e., local variations [8]. However, this flow will also destroy useful surface features if run too long. One of the main issues concerning this flow is if there is a stopping criterion for an optimal shape refinement. Several methods have been proposed in the past, one that adds a term to force the solution to remain close to the initial data [22], and the authors in [16] have studied a scale dependent stopping criteria implemented via a min-max curvature flow. In the present context, the stopping condition is given by the  $g$  function. So, the surface moves according to

$$\mathcal{S}_t = gH\vec{\mathcal{N}}. \quad (11)$$

Recall that the function  $g$  is an edge indicator, i.e., a nonincreasing function of the image gradient. Since we have already denoised the input image thereby improving the edge definition, the  $g$  function is computed as follows:

$$g(\mathbf{x}) = e^{-\alpha|\nabla I_D(\mathbf{x})|}, \quad \alpha > 0 \quad (12)$$

where  $I_D(\mathbf{x})$  is the denoised/enhanced image.

Our second objective is to steer the surface closer to the “true” edges in order to produce a better reconstruction. So, we rewrite (3) without the constant speed term here

$$\psi_t - gH|\nabla\psi| - \beta\nabla g \cdot \nabla\psi = 0 \quad (13)$$

where  $\beta$  is a nonzero constant. The first term smooths the surface while keeping it close to the edges and the second term,  $\beta\nabla g \cdot \nabla\psi$ , attracts the surface closer to the edge map. In the absence of a close enough initial condition, it is difficult to solve the above equation, 1) because it expresses the necessary condition for a nonconvex minimization problem, and 2) partly because we do not have the constant speed term [as in (3)] that ordinarily helps one to navigate closer to the true edges. In the present context, we do have a good initial condition to solve (13). The initial condition  $\psi(\mathbf{x}, t = 0)$  is given by the signed distance function computed off of the binarized image obtained from a rough segmentation. In other words, to obtain an accurate surface description of nuclei, we first use a quick and automatic scheme to arrive at a rough surface and then pull it closer to the true edges by solving (13). As an example, the result of applying this flow on a coarse binary segmentation is shown in Fig. 10. Surface rendered in Fig. 10(b) is not only closer to true edges but also described with sub-voxel accuracy.

#### A. Shape Refinement

Sometimes, there is substantial surface error due to an incorrect interpretation of the nuclear boundary by the watershed algorithm that is used for dividing clusters. In those cases, the surface of the nucleus occupies part of the background space between nuclei or even includes part of a neighboring nucleus. An example of this can be seen in Fig. 11(a) and (c).



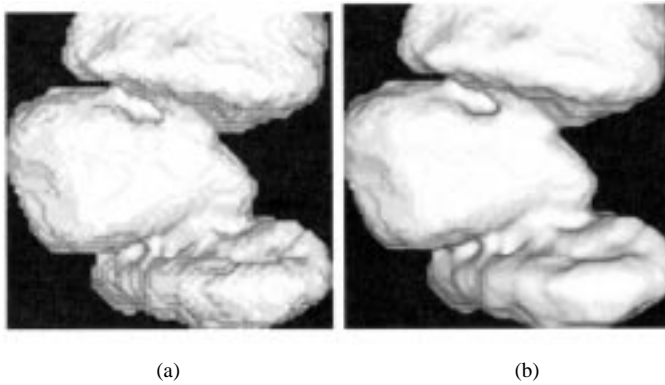


Fig. 10. Shape refinement; (a) Zero level set of the signed distance function computed on the rough segmentation of a cluster of cells, and (b) Geometric segmentation with  $\beta = 1$ .

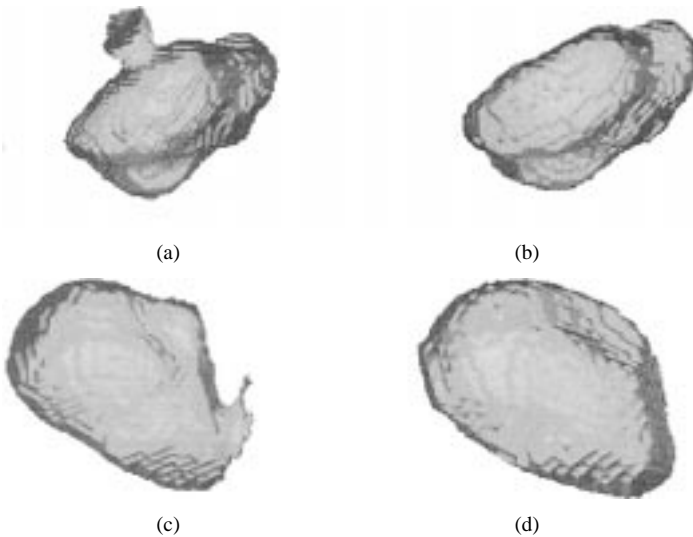


Fig. 11. Two examples of level set-based shape refinement. (a) Incorrectly segmented. (b) Corrected. (c) Incorrectly segmented. (d) Corrected.

A combination of two flows derived from the general (3) corrects that error: The first flow produces inward movement following the equation:

$$\psi_t - (-1 - \epsilon H)|\nabla\psi| = 0. \quad (14)$$

The term  $\epsilon H$  forces the front to remain smooth, and accelerates the front in high curvature parts of the front, generally corresponding to artifacts we want to eliminate. The outcome of this flow is a simplified, shrunk version of the original object, free from artifacts.

Then we apply the surface reconstruction flow

$$\psi_t - g\epsilon H|\nabla\psi| - \beta \nabla g \cdot \nabla\psi = 0 \quad (15)$$

that we already introduced earlier in this section. To prevent different fronts from collapsing into each other and losing their identity, we move each front independently, assigning them a trial value. If two regions collide based on the trial function values, the value of the actual function is changed by considering the values of other level set functions. Merger can be avoided by a simple max operator. Further details can be found in [32]. Fig. 11(b) and (d) show the effect of running the above combination of flows on surfaces in Fig. 11(a) and (c).

## VI. CONCLUSION

In this paper, we have presented a methodology to do various image analysis tasks that one typically encounters in the study of confocal microscope images. These tasks range from low-level feature-preserving noise elimination, nuclei to cell shape smoothing and reconstruction. In this work, we propose a unified geometric framework in which all of the aforementioned image analysis tasks are implemented efficiently as various interpretations of an underlying partial differential equation. We present results on testing our method on real confocal microscope images.

## REFERENCES

- [1] D. Adalsteinsson and J. A. Sethian, "A fast level set method for propagating interfaces," *J. Comp. Phys.*, vol. 118, no. 2, pp. 269–277, May 1995.
- [2] L. Alvarez, F. Guichard, P. L. Lions, and J. M. Morel, "Axioms and fundamental equations of image processing," *Arch. Rational Mechanics*, vol. 123, 1993.
- [3] H. Ancin, B. Roysam, T. E. Dufresne, M. M. Chesnut, G. M. Ridder, D. H. Szarowski, and J. N. Turner, "Advances in automated 3-D image analysis of cell populations imaged by confocal microscopy," *Cytometry*, vol. 25, pp. 221–234, 1996.
- [4] V. Caselles, F. Catte, T. Coll, and F. Dibos, "A geometric model for active contours," *Numerische Mathematik*, vol. 66, pp. 1–31, 1993.
- [5] V. Caselles, R. Kimmel, and G. Sapiro, "Geodesic active contours," presented at the ICCV'95, Cambridge, MA, 1995.
- [6] M. Czader, A. Liljeborg, G. Auer, and A. Porwit, "Confocal 3-dimensional DNA image cytometry in thick tissue sections," *Cytometry*, vol. 25, pp. 246–253, 1996.
- [7] P. Dean, L. Mascio, D. Ow, D. Sudar, and J. Mullikin, "Proposed standard for image cytometry data files," *Cytometry*, vol. 11, pp. 561–569, 1990.
- [8] M. Grayson, "The heat equation shrinks embedded plane curves to round points," *J. Differential Geometry*, vol. 26, pp. 285–314, 1987.
- [9] G. H. Heppner, "Cell-to-cell interaction in regulating diversity of neoplasms," *Seminars Cancer Biol.*, vol. 2, pp. 97–103, 1991.
- [10] T. Irinopoulou, J. Vassy, M. Beil, P. Nicolopoulou, D. Encaoua, and J. P. Rigaut, "Three-dimensional DNA image cytometry by conical scanning laser microscopy in thick tissue blocks of prostatic lesions," *Cytometry*, pp. 27:99–27:105, 1997.
- [11] M. Kass, A. Witkin, and D. Terzopoulos, "Snakes: Active contour models," *Int. J. Comput. Vision*, vol. 1, pp. 321–331, 1988.
- [12] S. Lelievre, V. M. Weaver, and M. J. Bissell, "Extracellular matrix signaling from the cellular membrane skeleton to the nuclear skeleton: A model of gene regulation," *Recent Prog. Hormone Res.*, vol. 51, pp. 417–432, 1996.
- [13] S. J. Lockett, D. Sudar, C. T. Thompson, D. Pinkel, and J. W. Gray, "Efficient, interactive, three-dimensional segmentation of cell nuclei in thick tissue sections," *Cytometry*, vol. 31, pp. 275–286, 1998.
- [14] R. Malladi, J. A. Sethian, and B. C. Vemuri, "A topology-independent shape modeling scheme," *SPIE: Geometric Meth. Comput. Vision II*, vol. 2031, pp. 246–258, 1993.
- [15] —, "Shape modeling with front propagation: A level set approach," *IEEE Trans. Pattern Anal. Machine Intell.*, vol. 17, pp. 158–175, Feb. 1995.
- [16] R. Malladi and J. A. Sethian, "Image processing: Flows under Min/Max curvature and mean curvature," *Graphical Models Image Processing*, vol. 58, no. 2, pp. 127–141, Mar. 1996.
- [17] —, "Level set methods for curvature flow, image enhancement, and shape recovery in medical images," in *Visualization and Mathematics: Experiments, Simulations, and Environments*, H. C. Hege and K. Polthier, Eds. Heidelberg, Germany: Springer-Verlag, 1997, pp. 329–345.
- [18] —, "A real-time algorithm for medical shape recovery," in *Proc. ICCV '98*, Mumbai, India, Jan. 1998, pp. 304–310.
- [19] K. Mikula, A. Sarti, and C. Lamberti, "Geometrical diffusion in 3-D echocardiography," presented at the ALGORITHM '97—Conf. Scientific Computing, West Tatra Mountains, Slovakia, 1997.
- [20] F. R. Miller and G. H. Heppner, "Cellular interactions in metastasis," *Cancer Metastasis Rev.*, vol. 9, pp. 21–34, 1990.

- [21] J. C. Mullikin, "The vector distance transform in two and three dimensions," *CVGIP: Graphical Models Image Processing*, vol. 54, no. 6, pp. 526–535, 1992.
- [22] N. K. Nordstrom, "Variational edge detection," Ph.D. dissertation, Dept. Elect. Eng., Univ. California, Berkeley, 1990.
- [23] C. Ortiz de Solórzano, E. Garcia Rodriguez, A. Jones, D. Pinkel, J. W. Gray, D. Sudar, and S. J. Loeckett, "Segmentation of confocal microscope images of cell nuclei in thick tissue sections," *J. Microscopy*, vol. 193, no. 3, pp. 212–226, 1999.
- [24] S. J. Osher and J. A. Sethian, "Fronts propagation with curvature dependent speed: Algorithms based on Hamilton–Jacobi formulations," *J. Computational Phys.*, vol. 79, pp. 12–49, 1988.
- [25] J. P. Rigaut, J. Vassy, P. Herlin, F. Duigou, E. Masson, D. Briane, J. Foucrier, S. Carvajal-Gonzalez, A. M. Downs, and A.-M. Mandard, "Three-dimensional DNA image cytometry by confocal scanning laser microscopy in thick tissue blocks," *Cytometry*, vol. 12, pp. 511–524, 1991.
- [26] B. M. ter Haar Romeny, Ed., *Geometry-Driven Diffusion in Computer Vision*. Norwell, MA: Kluwer Academic, 1994.
- [27] G. Sapiro, "Color snakes," Hewlett–Packard Lab., Tech Rep., 1995.
- [28] G. Sapiro, R. Kimmel, D. Shaked, B. B. Kimia, and A. M. Bruckstein, "Implementing continuous-scale morphology via curve evolution," *Pattern Recogn.*, vol. 26, no. 9, pp. 1363–1372, 1993.
- [29] A. Sarti, K. Mikula, and F. Sgallari, "Nonlinear multiscale analysis of 3-D echocardiographic sequences," *IEEE Trans. Med. Imag.*, 1997, submitted for publication.
- [30] A. Sarti, C. Ortiz, S. Lockett, and R. Malladi, "A unified geometric model for 3-D confocal image analysis in cytology," Lawrence Berkeley National Laboratory, Univ. California, Berkeley, LBNL Rep 41 740, Apr. 1998.
- [31] J. A. Sethian, "A review of recent numerical algorithms for hypersurfaces moving with curvature dependent flows," *J. Differential Geometry*, vol. 31, pp. 131–161, 1989.
- [32] J. A. Sethian, *Level set methods: Evolving interfaces in geometry, fluid mechanics, computer vision, and material science*. New York: Cambridge Univ. Press, 1997.
- [33] N. Sochen, R. Kimmel, and R. Malladi, "A general framework for low-level vision," *IEEE Trans. Image Processing (Special Issue on PDE's and Geometry-Driven Diffusion in Image Processing and Analysis)*, vol. 7, pp. 310–318, Mar. 1998.
- [34] T. Wilson, *Confocal Microscopy*. London, U.K.: Academic, 1990.



**Alessandro Sarti** received the Laurea degree in electronic engineering in 1991 and the Ph.D. degree in bioengineering, with a thesis in computational image analysis, from the University of Bologna, Bologna, Italy.

Since 1997, he holds a Post-Doctoral position at the Department of Mathematics, University of California, Berkeley, and Department of Mathematics, Lawrence Berkeley National Laboratory, University of California, Berkeley. His research interests include computer vision, partial differential equations, and

medical imaging.



**Carlos Ortiz de Solórzano** (M'99) was born in León, Spain, on June 4, 1967. He received a degree in telecommunication engineering in 1992 and a Ph.D. degree in telecommunication engineering (Biomedical Engineering Program) in 1996, both from the Universidad Politécnica de Madrid, Madrid, Spain.

From 1997 to 2000 he was a Postdoctoral Fellow at the Digital Microscopy and Imaging Group, Lawrence Berkeley National Laboratory, of the University of California, in Berkeley, CA. Currently

he is an Associate Professor in the Computer Sciences Department, Universidad Autónoma de Madrid. His research interests are in biomedical applications of computer vision and image processing.



**Stephen Lockett** received the Ph.D. degree in medical biophysics from the University of Birmingham, Birmingham, England, in 1987.

From December 1987 to November 1993, he was a Postdoctoral Fellow and then a Research Assistant Professor at the University of North Carolina, Chapel Hill. Since then he has been a Staff Scientist at the Lawrence Berkeley National Laboratory, CA. His research interests cover the fields of fluorescence microscopy and digital image analysis, with applications to understanding the

molecular mechanisms of cells within their natural tissue context. He has authored over 30 papers and has given several invited lectures.



**Ravikanth Malladi** received the B.Eng. degree with honors in electrical engineering and M.Sc. degree in physics from Birla Institute of Technology and Science, Pilani, India, in 1988. He received the M.S. degree in 1991 and the Ph.D. degree in 1993; both in computer vision from the University of Florida, Gainesville.

He is currently a Staff Computer Scientist and heads the image understanding efforts in the Department of Mathematics at the Lawrence Berkeley National Laboratory, University of California,

Berkeley. In the summer of 1985, he worked at the National Geophysical Research Institute, Hyderabad, India. During spring of 1988, he held a Research Assistant position with the semiconductor physics group in Central Electrical and Electronics Research Institute, Pilani, India. At the University of Florida he was a Research Assistant in the Center for Computer Vision and Visualization. From spring 1994 to Summer 1995, he was a Postdoctoral Fellow at Department of Mathematics, University of California, Berkeley, and Lawrence Berkeley Laboratory. His research interests are focused on medical and biomedical image processing, computational vision, shape modeling and recognition, computer graphics, and computer-aided machining.

Dr. Malladi was awarded the National Science Foundation (NSF) Postdoctoral Fellowship in Computational Science and Engineering in June 1994 and his work received best peer reviews and ranked the best paper at the Third European Conference on Computer Vision, Stockholm, Sweden, in May 1994.